

Article

Electromagnetic Characteristics Analysis and Structure Optimization of High-Speed Fuel Solenoid Valves

Liu Yang ^{1,2,3,*} , Tianxiong Gao ¹, Xinming Du ¹, Fugang Zhai ^{1,3}, Chang Lu ⁴ and Xiangdong Kong ^{1,3}¹ School of Mechanical Engineering, Yanshan University, Qinhuangdao 066004, China² State Key Laboratory of Fluid Power and Mechatronic Systems, Zhejiang University, Hangzhou 310027, China³ Hebei Heavy Machinery Fluid Power Transmission and Control Laboratory, Qinhuangdao 066004, China⁴ AVIC Changchun Control Technology Co., Ltd., Changchun 130102, China

* Correspondence: yangliu_ysu@ysu.edu.cn

Abstract: High-speed fuel solenoid valves (HFSVs) are the key control elements of aero-engine vane regulators. A strong electromagnetic force generated from the HFSVs is essential to achieve precise control over timing and quantification for fuel supply. In this paper, the Taguchi method is adopted to improve the HFSV's static electromagnetic characteristics. First, an electromagnetic model of the HFSV was established and experiments were conducted to modify and validate the model. Effects of key structural factors on the static electromagnetic characteristics of the HFSV are then investigated via the finite element method (FEM). Based on the optimization, an HFSV prototype is finally manufactured and tested. The experiment results are in good agreement with those of the simulations. It provides a significant guideline for the manufacturing process of such HFSVs.

Keywords: high-speed solenoid valve; static electromagnetic force; Taguchi method; FEM



Citation: Yang, L.; Gao, T.; Du, X.; Zhai, F.; Lu, C.; Kong, X.

Electromagnetic Characteristics Analysis and Structure Optimization of High-Speed Fuel Solenoid Valves. *Machines* **2022**, *10*, 964. <https://doi.org/10.3390/machines10100964>

Academic Editors: Qun Chao, Ruqi Ding and Min Cheng

Received: 21 September 2022

Accepted: 19 October 2022

Published: 21 October 2022

Publisher's Note: MDPI stays neutral with regard to jurisdictional claims in published maps and institutional affiliations.



Copyright: © 2022 by the authors. Licensee MDPI, Basel, Switzerland. This article is an open access article distributed under the terms and conditions of the Creative Commons Attribution (CC BY) license (<https://creativecommons.org/licenses/by/4.0/>).

1. Introduction

Due to the rapid growth of China's national economy, the number of aircraft in service has increased dramatically with the development of civil aviation. China's civil aviation passenger volume is predicted to be second only to the United States in the next 20 years [1–5]. Along with the pursuit of faster, safer and more convenient demands, people are paying more attention to flight safety. As to the aircraft failure, more than 50% of accidents are reported to come from the engines, while the gas path failure could account for 90% of the total engine failure [6]. High speed fuel solenoid valve (HFSV) is an important control element in the aerospace field, which is mainly used in aero-engine guide vane regulating systems [7,8]. With the help of HFSV, the real-time and accurate adjustment of stator blade angle could be achieved to improve the surge margin of compressors and expand the stable working range of engines, which ensures the safe and reliable operation of aero-engines. The improved requirements in aircraft stability and reliability require strong static electromagnetic forces generated from HFSV to meet the demands for the precise control of fuel. Therefore, studying for the influence of valve structure factors on static electromagnetic characteristics is of great significance.

As for HFSVs, the static electromagnetic force is generated from the interactions between armature current and the magnetic core. At present, the static characteristic of HFSV is mostly researched by the magnetic field analysis method and finite element method (FEM) [9,10]. In [11], influence of the pole shoe shape, guide sleeve thickness, magnetic material, iron core structure and other parameters of the electromagnet on the static electromagnetic force was analyzed and the optimal structural parameters of the electromagnet was obtained. In [12], the effects of structural parameters of a solenoid valve pole shoe on static characteristics were determined by FEM, and the optimal structural parameters of a pole shoe were determined by evaluation strategy algorithm. In [13], the armature structural parameters of the solenoid valve on the static electromagnetic force

were investigated and optimized by genetic algorithm. In [14], iron core was optimized through the study of the influence of the core cross-sectional area and ampere turns on static electromagnetic characteristics. In [15], a mathematical model of electromagnetic force of a high-speed solenoid valve (HSV) was established, and the influence of valve key parameters on an electromagnetic force of a common rail injector was further studied. Besides the influence of key parameters (e.g., magnetizer height, width of working air gap and damping hole angle) on the working characteristics of an electromagnetic injector, driving current and structural parameters of a solenoid valve on the static electromagnetic characteristics were also implemented [16–18]. Considering the magnetic saturation phenomenon, an electromagnetic mathematical model of the high-speed solenoid valve was established [19].

The above study for influence of gap and material magnetoresistance on the electromagnetic characteristics were mainly based on univariate analysis. Multi-objective optimization technology was used to optimize the dynamic response characteristics of HSV [20–22]. In [20], optimization of five selected key factors, which is related to the dynamic response characteristics of high-speed solenoid valves, was achieved by the Kriging model. In [21], optimal parameters of a proportional electromagnet were found by studying the influence of the basin mouth depth. According to the dynamic behavior of proportional electromagnets of different models, a natural model test method was used to fit the measurement on the physical object, and natural model experiments were proposed to verify the dynamic properties [22].

Great efforts have been devoted to the optimization of static electromagnetic forces. However, most of them are limited to the improvement of static electromagnetic forces at a certain position in the working stroke. To the best of our knowledge, the multi-objective optimization of static electromagnetic forces at different working positions has not been studied under the full working cycle.

In this paper, the static characteristics of the HFSV for blade regulator are studied and optimized. Firstly, the working principle of the HFSV is introduced. Secondly, the mathematical model of the HFSV is established and corrected by experiments. On this basis, the influence of a single factor on static electromagnetic force is analyzed. Thirdly, the Taguchi method is used for the optimization of static electromagnetic force at different working positions in the working stroke, considering the coupling effect of multiple factors on the static electromagnetic force. Finally, a sample HFSV is manufactured and tested.

2. Structure and Working Principle

The HFSV introduced in this paper is a normally closed valve. This is an on–off valve that relies on the spring return. The flow of the valve is 1.5 L/min when entrance pressure difference is 1 MPa. The structure, which is divided into electromagnet and valve body, is shown in Figure 1a. The electromagnet part is mainly composed of the screw plug, plug frame, shell, coil winding, skeleton, limit core, guide sleeve, armature and iron sealing components. The armature is guided by the axial sliding of the sealing iron, the screw plug is connected with the plug frame through the screw thread. An adjustable non-working air gap δ between the screw thread rotation and the limiting core could be formed in the screw plug. The working air gap h is formed between the armature and the limiting core.

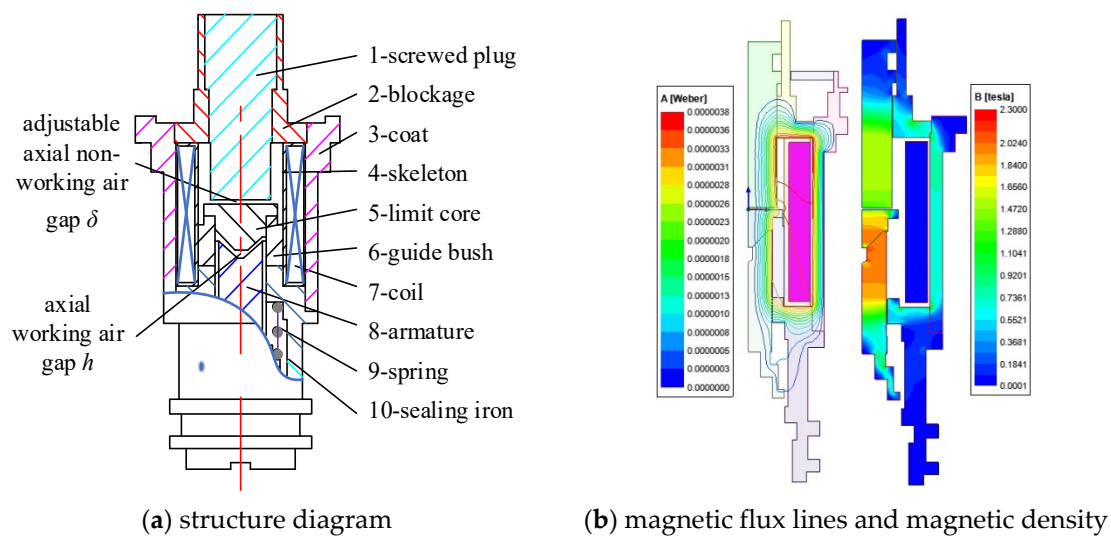


Figure 1. Structure diagram and magnetic field distribution of the HFSV.

When the coil is excited, a closed magnetic circuit will be formed along the minimum path of magnetoresistance, through the magnetic components of a screw plug, limit core, armature, iron seal, shell and screwed plug. That is shown in Figure 1b. Axial electro-magnetic attraction will be generated in the axial working air gap. Then, the armature overcomes the forces of spring, friction and damping, and then the valve begins opening. In the state of power failure, the armature would be reset under the action of spring force. The armature is pressed and reaches to the valve seat to keep the valve port be closed.

Six different measured positions of surface magnetic density of the HFSV are shown in Figure 2. The real magnetic density of the HFSV was measured by Gauss meter and compared with the simulation values, as shown in Table 1. It can be seen that the simulation results are in good agreement with the test results, which verified the correctness of the established simulation model.

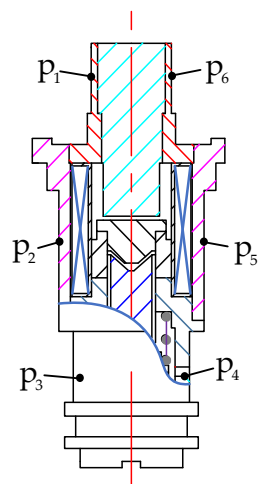


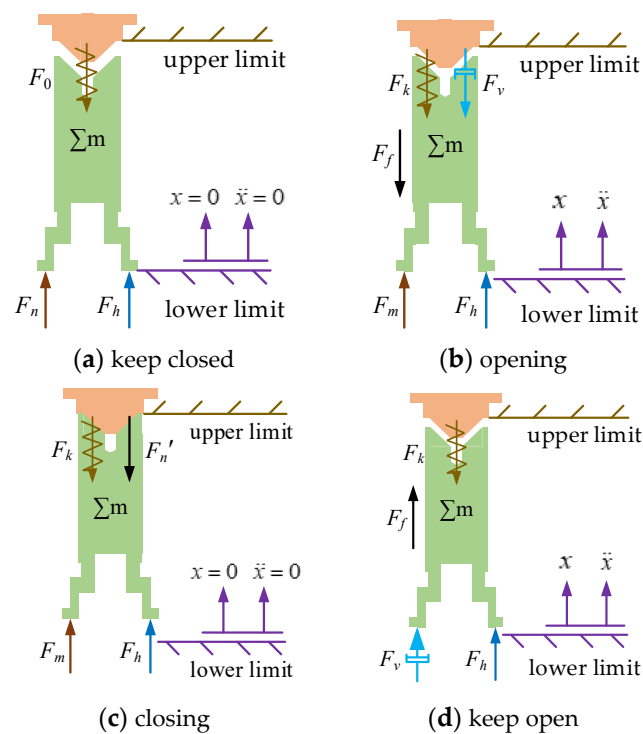
Figure 2. The measured positions of surface magnetic density of the HFSV.

Table 1. The simulation value compared with experimental results.

Test Point	Simulation	Experiment
P1	0.011 T	0.013 T
P2	0.552 T	0.572 T
P3	0.022 T	0.030 T
P4	0.031 T	0.021 T
P5	00561 T	0.541 T
P6	0.015 T	0.016 T

3. Dynamic Mathematical Model of HFSV

The force of armature in the working state is the combined action of electromagnetic force F_m , spring force F_k , friction force F_f and damping force F_v . The gravity of armature assembly Σmg is very small, which can be ignored. The armature undergoes four states during the working process, which are kept closed, opening, kept open and closing. The force analysis of armature in the four states is shown in Figure 3.

**Figure 3.** Stress analysis diagram of armature in each state.

The force analysis of the armature closing state is shown in Figure 3a. The coil is not excited, the electromagnetic force F_m is zero, and the spring preload F_0 is greater than the hydraulic pressure F_h at the initial position, so that the armature is statically pressed on the valve seat. The force balance equation is:

$$F_n + F_h - F_0 = 0 \quad (1)$$

where F_n is the force of valve seat on armature (N); F_h is the hydraulic pressure (N); F_0 is the spring preload (N), 4.5 N.

The force analysis of armature opening state is shown in Figure 3b. When the coil is excited, the electromagnetic force F_m is not zero, electromagnetic force F_m and hydraulic pressure F_h overcome the spring force F_k and friction F_f and damping force F_v . Then the valve port opens, and then the dynamic equation is:

$$\Sigma m \ddot{x} = F_m + F_h - F_k - F_f - F_v = F_m + F_l \quad (2)$$

where m is the mass of armature assembly (kg); \ddot{x} is acceleration of armature (N); F_k is spring force (N); F_f is the friction force of armature (N); F_v is damping force of armature (N); F_l is load force on armature.

The force analysis with the valve port kept open is shown in Figure 3c. After the opening state, the armature moves upward, and the air gap becomes zero. The coil continues to be excited, the electromagnetic force F_m is not 0, the electromagnetic force F_m and the hydraulic pressure F_h are greater than the spring force F_k , the valve port remains open, and the force balance equation is:

$$0 = F_m + F_h - F_k - F_n' \tag{3}$$

where F_n' is the force of upper limit on armature (N).

The stress analysis of the armature return state is shown in Figure 3d. The coil is not excited. The electromagnetic force F_m is 0. The spring force F_k overcomes the hydraulic pressure F_h to make the armature closed, and dynamic equation is:

$$\Sigma m\ddot{x} = F_h + F_f + F_v - F_k \tag{4}$$

The working load of the spring can be expressed as:

$$F_k = F_0 + kx \tag{5}$$

where k is spring coefficient (N/mm), 500 N/mm; x is displacement of armature (mm).

The armature generates friction between the sealing iron and the inner wall of the guide sleeve during the action, and forming a friction force against the armature. Because the valve body is immersed in fuel medium, the friction coefficient is small, and the quality of armature assembly is also small, the friction of armature can usually be ignored in previous studies. In this paper, the friction F_f is ignored when analyzing the dynamic characteristics of high-speed solenoid valve.

The damping force of the armature assembly is the viscous resistance between the armature assembly and the fuel medium during the movement. The calculation expression is:

$$F_v = \zeta v \tag{6}$$

where ζ is the damping coefficient of velocity (N/(m/s)); v is the speed of armature (m/s).

4. Electromagnetic Modeling

Magnetic equivalent circuit of the HFSV is divided by magnetic circuit segmentation method, as depicted in Figure 4. The red virtual line represents the path of the main flux Φ . NI is defined as the magnetomotive force of the electrified coil.

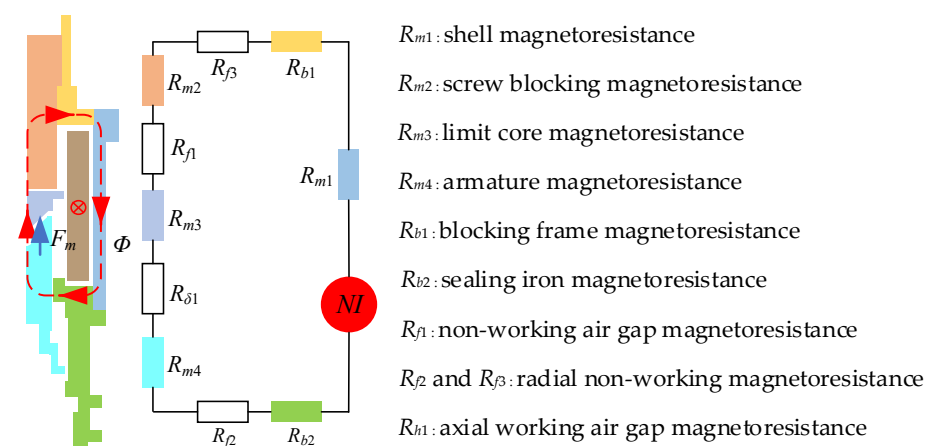


Figure 4. Magnetic equivalent circuit of the HFSV.

It can be found from Figure 2, due to all the magnetoresistances being series connected, that the total magnetoresistance ΣR_c can be calculated as below.

$$\Sigma R_c = \Sigma R_m + R_h + \Sigma R_f + \Sigma R_b \quad (7)$$

where ΣR_m is the axial reluctance of magnetic element (H^{-1}); R_h is working air gap magnetoresistance (H^{-1}); ΣR_f is non-working air gap magnetoresistance (H^{-1}); ΣR_b is a magnetic element with radial magnetoresistance (H^{-1}). The specific sub-items of each reluctance are $\Sigma R_m = R_{m1} + R_{m2} + R_{m3} + R_{m4}$, $\Sigma R_f = R_{f1} + R_{f2} + R_{f3}$, $\Sigma R_b = R_{b1} + R_{b2}$, $R_h = R_{h1}$.

The axial magnetoresistance of magnetic elements is:

$$R_{mi} = \frac{L_{mi}}{\mu_i \cdot S_{mi}} \quad (8)$$

where μ_i is the permeability of the magnetic material (H/m); L_{mi} is magnetic element length (mm); S_{mi} is the cross-sectional area of magnetic components (mm^2).

The two parallel circular planar non-working air gap reluctance R_{f1} between the limit core and the screw plug is deduced as:

$$R_{f1} = \frac{\delta}{\mu_0 \cdot S_0} \quad (9)$$

where δ is the length of non-working air gap (mm); μ_0 is vacuum permeability (H/m), and equals to $4\pi \times 10^{-7}$ H/m; S_0 is non-working air gap flux area (mm^2).

The non-working air gap magnetoresistance R_{f2} formed by radial concentric annular surface between armature and seal is deduced as:

$$R_{f2} = \frac{\ln(r_{f2}/r_{f1})}{2\pi \cdot \mu_0 \cdot L_{f1}} \quad (10)$$

where r_{f1} is the inner diameter of radial air gap annular plane between armature and sealing iron (mm); r_{f2} is the outer diameter of radial air gap annular plane between armature and sealing iron (mm); L_{f1} is the axial thickness of radial air gap of armature and sealing iron (mm).

The non-working air gap reluctance R_{f3} formed by the radial concentric annular surface between the screw plug and the plug frame is deduced as:

$$R_{f3} = \frac{\ln(r_{f4}/r_{f3})}{2\pi \cdot \mu_0 \cdot L_{f2}} \quad (11)$$

where r_{f3} is the inner diameter of the radial air gap between the screw plug and the plug frame (mm); r_{f4} is the outer diameter of the annular surface of the radial air gap between the screw plug and the plug frame (mm); L_{f2} is the axial thickness of the radial air gap between the screw plug and the plug frame (mm).

The magnetoresistance R_b formed by the radial concentric annular surfaces of screw plug and iron seal is deduced as:

$$R_b = \frac{\ln(r_{bi}/r_{bo})}{2\pi \cdot \mu_i \cdot L_{bi}} \quad (12)$$

where r_{bi} is the inner diameter of the annular surface of the radial magnetic material between the screw plug and iron seal (mm); r_{bo} is the outer diameter of the annular surface of the radial magnetic material between screw plug and iron seal (mm); L_{bi} is the axial thickness of the radial magnetic material of screw plug and iron seal (mm).

The magnetoresistance R_{h1} of axial conical surface working air gap between armature and limiting core can be deduced as:

$$R_{h1} = \frac{1}{\mu_0 \left(\frac{\pi d_c^2}{4h \sin^2 \alpha} - \frac{0.157 d_c}{\sin^2 \alpha} + 0.75 d_c \right)} \quad (13)$$

where d_c is the diameter of conical cylinder (mm); α is the cone angle of the conical surface ($^\circ$); h is the cone axial spacing (mm).

The flux Φ in the magnetic circuit is calculated as:

$$\Phi = \frac{NI}{\Sigma R} \quad (14)$$

where Φ is magnetic flux (Wb).

Thus, assuming that the magnetic flux is uniformly distributed on the conical surface of the armature, the axial electromagnetic force F_m of the armature can be calculated as:

$$F_m = \frac{\Phi^2}{2\mu_0 \cdot S_{m4}} \quad (15)$$

where F_m is the electromagnetic force of the armature (N); S_{m4} is the radial cross-sectional area of armature (mm^2).

5. FEM Modeling and Experimental Modification

5.1. FEM Modeling

The finite-element method (FEM), which considers accurate geometrical shapes, can provide accurate results. Therefore, FEM was preferred for the investigation of the HFSV. According to the actual structure size of coil and magnetic components in HFSV, the proportional model was built in the static electromagnetic field. Taking the magnetic leakage into consideration, the whole entity of the valve was set as a balloon boundary, and the calculation domain area is established, as shown in Figure 5a. A triangular element was selected to mesh the model adaptively, and the mesh refinement is carried out at the place where the magnetic field intensity changes greatly, involving the working air gap h , the non-working air gap δ between screw plug and limiting core, and radial air gap between armature and sealing iron, as shown in Figure 5b.

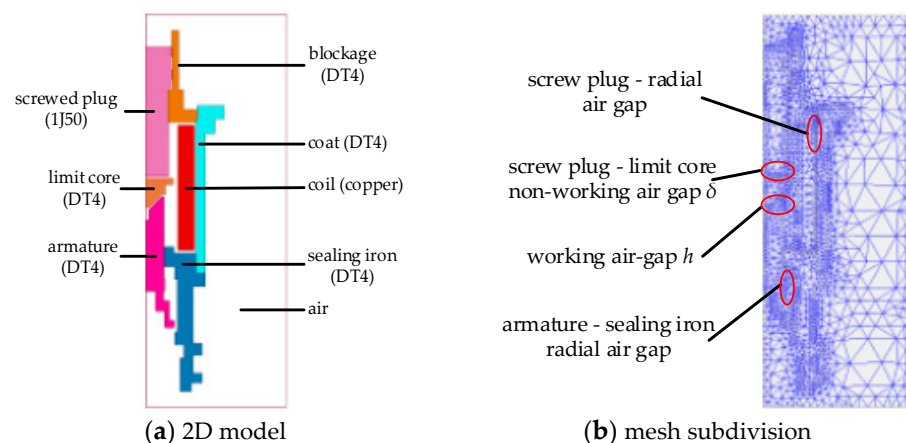


Figure 5. Static magnetic field model and meshing of valve.

The magnetization curves of DT4 and 1J50 are shown in Figure 6. The material of DT4 is high-quality steel which is commonly used soft magnetic material in electromagnetic components. 1J50 is Fe-Ni soft magnetic alloy. They have fine magnetic property and are

widely used in solenoid valve. The coil is applied as the excitation input terminal. The excitation condition is 710 ampere-turn, and the excitation current range is 0~950 mA.

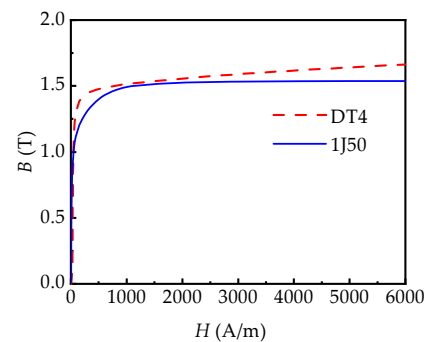


Figure 6. Magnetization curves of soft magnetic materials DT4 and 1J50.

5.2. Experimental Modification

A serial assistant program was used to gather dates. As shown in Figure 7, the test bench is composed of the tested HFSV, pull-pressure sensor, displacement sensor, stepper motor, host, DC power supply, motor drive module and controller. The right end of the armature and pull-pressure sensor is fixedly connected by a short screw rod. The stepper motor at the leftmost end, controls the position of the pull-pressure tension bracket through a ball screw. The position of the pull-pressure sensor could be adjusted through the sliding rail on the base under action of step motor, realizing the relative position change between the armature and the limiting core. It can adjust the relative distance between the sensor's holder and the solenoid valve. Voltage signals at different working air gap (i.e., relative distance) and excitation currents are collected by pull-pressure sensor. The signals can be converted into the static electromagnetic force, which can acquire static electromagnetic force with a different working air gap. The indicators of the experimental device are shown in Table 2.

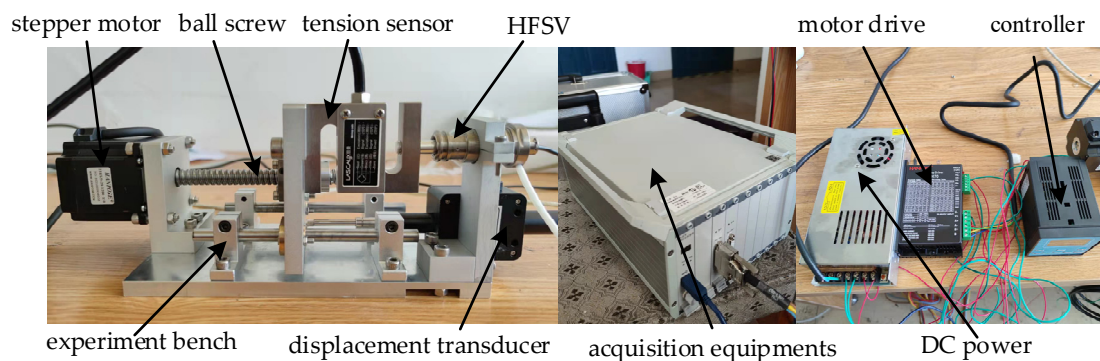


Figure 7. HFSV electromagnetic force test bench.

Table 2. Specifications of the experimental system.

Item	Value
DC power supply	24 V
Current	10 A
Power	250 W
divisions of pull-pressure sensor	2000
Displacement of core	0~0.3 mm

The test and simulation values of armature static electromagnetic force with different working air gap h are shown in Figure 8.

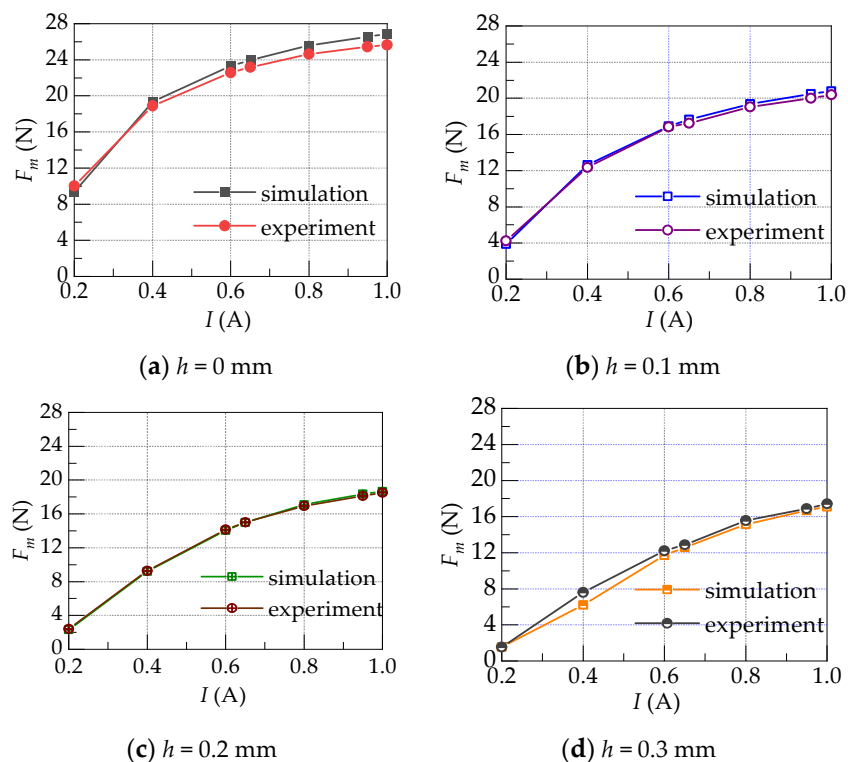


Figure 8. Test and simulation results of the static electromagnetic force along with the coil exciting current under different air gaps.

When the h is kept constant, the static electromagnetic force of the armature increases with the increment of the coil excitation current. When the coil excitation current keeps constant, the static electromagnetic force increases as the working air gap h decreases. The maximum error between simulation and test values is 6.7%. Thus, it is believed that the established HFSV’s static electromagnetic model is correct and can accurately simulate the static electromagnetic force.

6. Key Influence Factors on Static Electromagnetic Characteristic

The study of static characteristics is the foundation and steady state of the dynamic response. Base on this, the influence of key parameters on the static characteristics of HFSV was studied. The structural parameters of HFSV electromagnet components are shown in Figure 9.

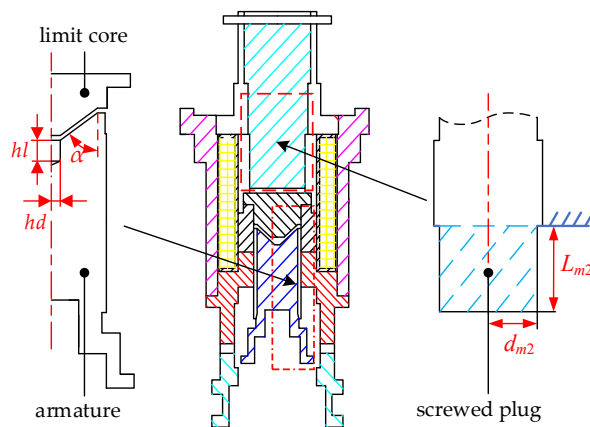


Figure 9. Key structural parameters of the HFSV.

The length and radius of the plug screw entry section are L_{m2} and d_{m2} , which can be converted into the magnetic flux cross-sectional area S_{m2} and the non-working air gap length δ . And the key structural parameters, which is between the armature and limiting core, are those of the conical magnetic pole angle α , armature opening radius hd and hole depth hl .

Magnetic circuit was firstly chosen to investigate the influence of various key factors on the static electromagnetic force. The variation range of the above factors (i.e., magnetic flux cross section area, non-working air gap length, cone angle of armature magnetic pole surface, radius of opening hole of armature and hole depth of armature) is shown in Table 3. Univariate analysis was adopted, which is when a certain factor variable is investigated, the other parameters will keep constant.

Table 3. Variation range of key structural parameters.

Parameter	Description	Unit	Fiducial Value	Range
S_{m2}	magnetic flux cross section area	mm ²	39.6	25.70~39.59
δ	non-working air gap length	mm	0.2	0~0.3
α	cone angle of armature magnetic pole surface	°	45	30~90
hd	radius of opening hole of armature	mm	0.5	0.5~1
hl	hole depth of armature	mm	1.5	1~5

6.1. Magnetic Flux Cross Section Area

Six groups of static electromagnetic force under different magnetic flux cross-sectional area S_{m2} were obtained by adjusting the magnetic pole radius d_{m2} , as shown in Figure 10. In this study, the range of S_{m2} was set to 25.70~39.59 mm². Under the same working air gap, the static electromagnetic force F_m of the armature decreases with the decrease in S_{m2} . This might be attributed to the excessive saturation of the magnetic induction intensity in the spiral section.

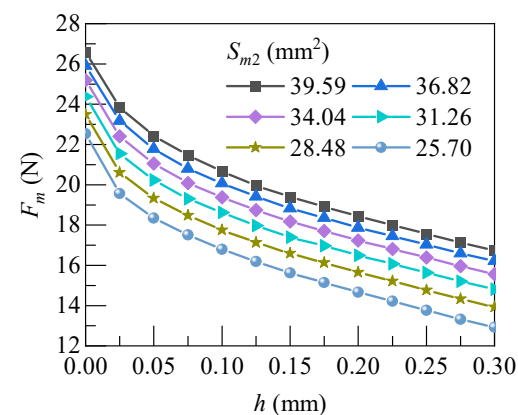


Figure 10. Static electromagnetic force varies with S_{m2} .

6.2. Non-Working Air Gap Length

After the connection of screw thread with the plug frame, the non-working air gap δ between the screw thread and the limiting core changed with adjustment of the length L_{m2} . Changing of δ in 0~0.3 mm resulted in the adjustment of the static electromagnetic force on the armature. Variation curves of the static electromagnetic force under different value of δ is shown in Figure 11.

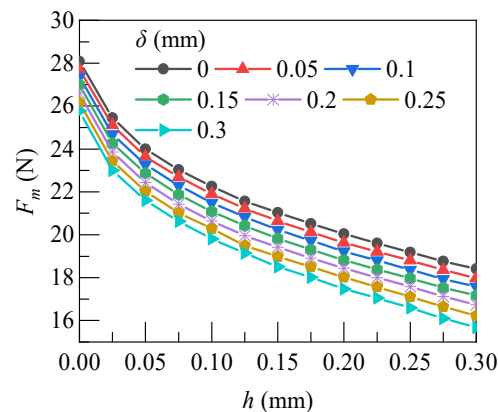


Figure 11. Static electromagnetic force varies with δ .

The curves showed that the static electromagnetic force F_m of the armature decreased with the increase in the non-working air gap δ under the same working air gap. From Formula (3), with the increase in the adjustable δ , the adjustable non-working air gap reluctance R_{f1} increases. When the coil excitation current is constant, the magnetic induction intensity in the magnetic circuit decreased, and resulted in the armature static electromagnetic force F_m decreasing.

6.3. Angle of Conical Magnetic Pole

The shape of the armature magnetic pole surface was designed as a cone, which makes the trend of the static electromagnetic force curve flatter. The reference value of conical polar angle α is 45° , and the adjustment range is 30° – 90° . The static electromagnetic force under the change of conical polar angle α was obtained by the model, as shown in Figure 12. Within this working stroke range, the static electromagnetic force F_m of the armature increased with the increase in the magnetic polar cone angle α . The increase trend decreased with the increase in the equivalency of the polar cone angle α . Therefore, the dynamic response performance of the solenoid valve could be improved by adjusting the cone angle α of the magnetic pole to match the reaction characteristics.

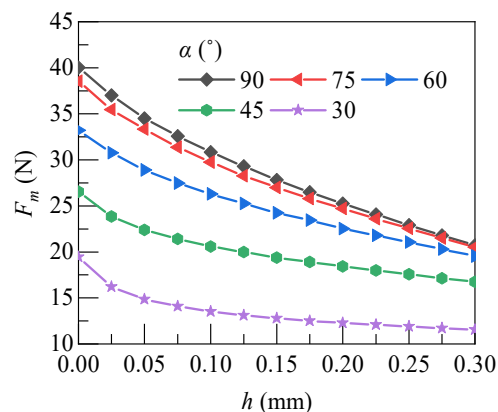


Figure 12. Static electromagnetic force varies with α .

6.4. Opening Size of Armature

As a moving part of HFSV, the armature electromagnetic force has direct influence on the dynamic response characteristics of armature. Thus, the influence of the hole size parameters on the static electromagnetic force of the armature was studied. The hole radius hd is 0.5 mm, the hole depth hl is 1.5 mm, the hole radius hd is 0.5–1 mm and the hole depth hl is 1–5 mm. The static electromagnetic force with the change of the hole radius hd and the hole depth hl was recorded, as shown in Figure 13.

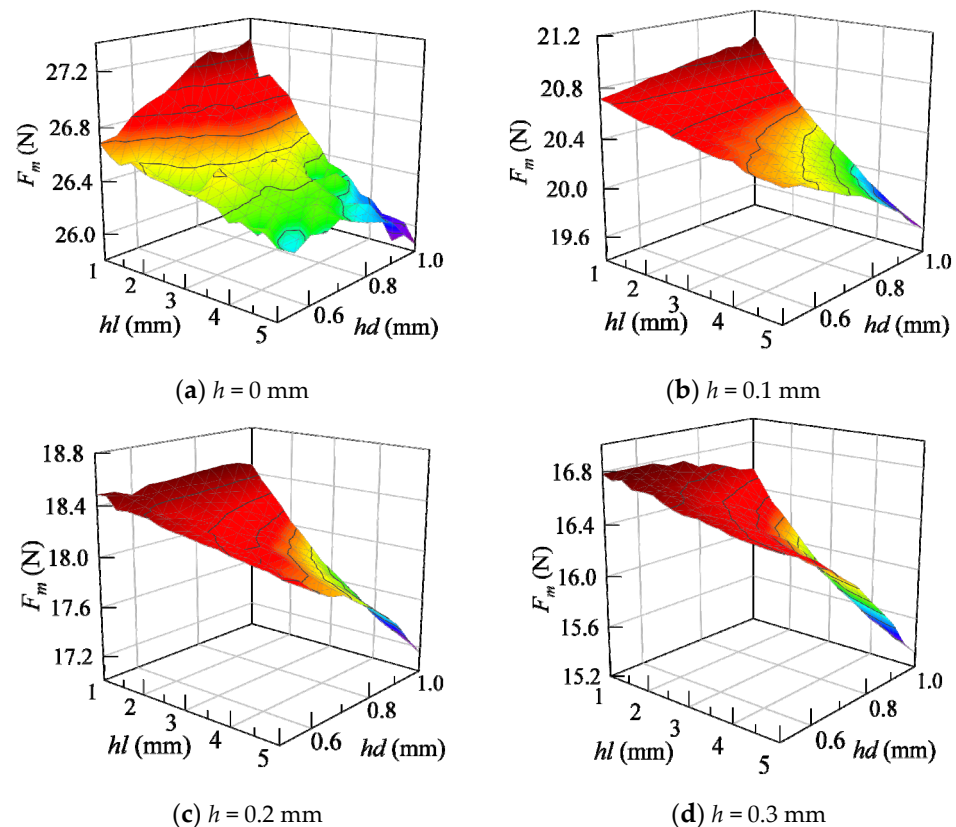


Figure 13. Static electromagnetic force along with opening radius and depth.

Figure 13 shows that the static electromagnetic force F_m under each working air gap h decreased with the increase in hl and hd . That's because the magnetic induction intensity of the ring area at the upper end of the armature reaches saturation as hd and hl grow. Additionally, reduction of the contact area resulted in the decrease in the static electromagnetic force F_m of the armature. However, the magnetic induction line was almost unable to pass the opening at the upper end of the armature, resulting in the limited variation of the static electromagnetic force F_m of the armature.

7. Taguchi Method Based Structural Optimization

The Taguchi method can be used to realize multi-objective optimization design [23–26]. By establishing an orthogonal table, the results of multi-objective optimization design parameters can be searched in less test time. The core idea of the Taguchi method is to apply the robust design to the product [25–28]. To optimize the products, it is necessary to look for the best combination of controllable factors, which could make the response variables more in line with the test requirements.

The specific calculation process of the Taguchi method is as follows:

The total mean of all tests:

$$M(S) = \frac{1}{n} \sum_{i=1}^n S_i \quad (16)$$

where $M(S)$ is the total mean; i is the number of tests; S_i is the result of the experiment i ; n is the number of orthogonal experiments.

Average value analysis can be expressed as:

$$M_{X(j)}(S) = \frac{1}{\tau} \sum_{i=1}^{\tau} S_i \quad (17)$$

where $M_{X(j)}(S)$ is the average of the optimization objectives at the level j of the specific control factor X ; X is a specific control factor; j is a certain level of the specific control factor; τ is the test result data of a specific control factor at this level.

Analysis of variance is:

$$SSD_X(S) = \frac{1}{N} \sum_{j=1}^N [M_{X(j)}(S) - M(S)]^2 \tag{18}$$

where $SSD_X(S)$ is variance of optimization object of factor X ; n is the level number. SS_0 , SS_1 , SS_2 and SS_3 are variance of optimization object of factors, which is $SSD_X(S)$ in Equation (12).

In the above single-factor analysis, the levels and ranges of the optimization variables of the experimental design model are determined. The number of test calculations is set to 9. The model of HFSV was numerically simulated according to the test scheme. The number of coil excitation turns is 674.5 A. The factors and levels of test design optimization variables are shown in Table 4.

Table 4. Factors level of the key influence parameters.

Parameter	Unit	Level 1	Level 2	Level 3
Magnetic flux cross section area S_{m2}	mm ²	25.7	32.65	39.6
Non-working air gap length δ	mm	0	0.15	0.3
Cone angle of armature magnetic pole surface α	°	30	60	90
Radius of opening hole of armature hd	mm	0.5	0.75	1
Hole depth of armature hl	mm	1	3	5

The test matrix and finite element simulation results are shown in Table 5. The average test values under the four different working air gaps are 29.06 N, 21.35 N, 17.87 N and 15.35 N, respectively. The proportion of the influence of optimization variables on the static electromagnetic force under four working air gaps is shown in Table 6. In this table, when $h = 0$ mm, the proportion of α is the largest, so it can be obtained that its influence on the electromagnetic force is the largest at the suction position, so the angle with large electromagnetic force is preferred. Similarly, in other positions, the influencing factors with a large proportion are preferentially selected, and then the parameters that can generate a large electromagnetic force are selected according to their influence law on the electromagnetic force.

Table 5. Test matrix and finite element analysis results.

Test Times	Test Matrix					F_{m0} (N)	F_{m1} (N)	F_{m2} (N)	F_{m3} (N)
	S_{m2} (mm ²)	δ (mm)	α (°)	hd (mm)	hl (mm)				
1	1 (25.7)	1 (0)	1 (30)	1 (0.5)	2 (3)	16.53	10.91	9.96	9.4
2	1	2 (0.15)	2 (60)	2 (0.75)	1 (1)	29.67	22.03	17.97	15.11
3	1	3 (0.3)	3 (90)	3 (1)	3 (5)	32.83	22.5	17.4	13.91
4	2 (32.65)	1	2	3	1	33.33	25.57	21.6	18.76
5	2	2	3	1	2	38.16	28.78	23.28	19.09
6	2	3	1	2	3	17.06	11.22	10.22	9.6
7	3 (39.6)	1	3	2	3	41.29	32.01	26.66	22.77
8	3	2	1	3	2	19.66	13.49	12.2	11.43
9	3	3	2	1	1	32.98	25.61	21.54	18.08

Table 6. Proportion of influence of optimization variables on static electromagnetic force at four working air gaps.

Variable	$h = 0 \text{ mm}$		$h = 0.1 \text{ mm}$		$h = 0.2 \text{ mm}$		$h = 0.3 \text{ mm}$	
	SS_0	Specific Gravity (%)	SS_1	Specific Gravity (%)	SS_2	Specific Gravity (%)	SS_3	Specific Gravity (%)
S_{m2}	4.22	7.68	4.67	7.68	4.33	11.85	3.67	16.65
δ	1.28	2.55	1.55	2.55	1.53	4.18	1.63	7.38
α	68.85	76.75	46.73	76.75	25.76	70.56	13.83	62.77
hd	0.10	0.56	0.34	0.56	0.32	0.89	0.23	1.03
hl	9.56	12.46	7.59	12.46	4.57	12.52	2.68	12.18

The influence trend of five variables on the static electromagnetic force F_m under four working air gaps is shown in Figure 14. It can be seen that the most obvious variable affecting the static electromagnetic force is the cone angle α , followed by the depth of the armature opening hole hl , the magnetic flux cross-sectional area S_{m2} , the length of the non-working air gap δ and the radius of the armature opening hole hd .

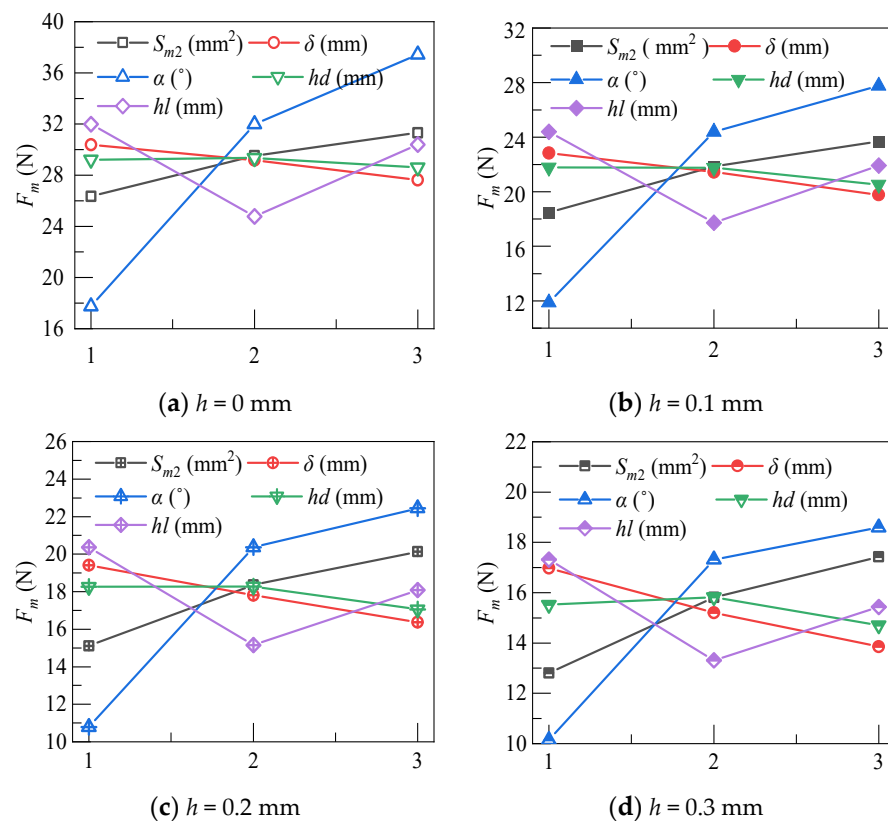


Figure 14. The influence trend chart of five optimization variables on static electromagnetic force.

The optimal structural design factors combination for the maximum static electromagnetic force is S_{m2} (3) δ (1) α (3) hd (2) hl (1). Meanwhile, the optimized HFSV prototype was manufactured and tested. In Figure 15, the experimental value is compared with the simulation under different working air gap. The experiment results are in good agreement with the simulation ones. The results before and after optimization are shown in Table 7. It can be found that the static electromagnetic forces are increased by 60.65%, 61.56%, 51.04% and 42.48%, when the working air gap position is 0 mm, 0.1 mm, 0.2 mm and 0.3 mm, respectively.

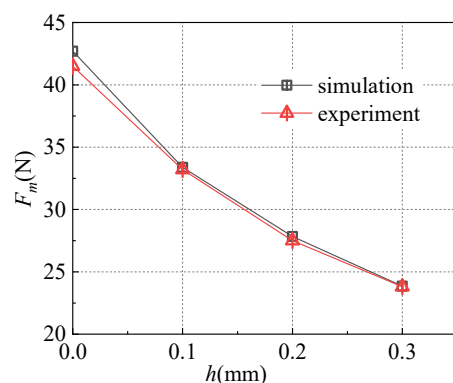


Figure 15. The experimental value is compared with the simulation under different working air gap.

Table 7. Simulation results of static electromagnetic force before and after optimization.

Working Air Gap (mm)	0	0.1	0.2	0.3
Electromagnetic force before optimization (N)	26.58	20.66	18.43	16.74
Optimized electromagnetic force (N)	42.70	33.38	27.84	23.85
Increase percentage (%)	60.65	61.56	51.04	42.48

8. Conclusions

In this paper, the static electromagnetic characteristics of HFSV were studied and optimized based on the Taguchi method. From the deduced axial electromagnetic force acting on the armature and FEM simulation results, five key influence parameters (i.e., magnetic flux cross-sectional area S_{m2} , non-working air gap length δ , conical magnetic pole angle α , armature opening radius hd and hole depth hl), were determined and the effects on the electromagnetic characteristics were obtained. The Taguchi method was adopted to the structural optimization by considering the coupling effect of the multiple factors at four locations in the working stroke. The range of armature's electromagnetic force increases about 42.48~61.56% at the working air gap position of 0~0.3 mm. The response speed of HFSV is also improved after the optimization of the electromagnetic force. The response speed of the valve is 2.01 ms and 1.63 ms before and after optimization, which is increased by 18.9%. The simulation and experimental results showed good agreement.

Author Contributions: Conceptualization, L.Y. and T.G.; methodology, L.Y.; software, X.D.; validation, L.Y., T.G. and X.D.; formal analysis, T.G. and X.D.; investigation, F.Z.; writing—original draft preparation, T.G. and X.D.; writing—review and editing, L.Y., F.Z. and X.K.; project administration, C.L.; funding acquisition, L.Y. All authors have read and agreed to the published version of the manuscript.

Funding: This research was funded by Open Foundation of the State Key Laboratory of Fluid Power and Mechatronic Systems (grant number GZKF-202124).

Institutional Review Board Statement: Not applicable.

Informed Consent Statement: Not applicable.

Data Availability Statement: Not applicable.

Conflicts of Interest: The authors declare no conflict of interest.

References

1. Wu, G. A Trio of Commercial Aircraft Developments in China. *Engineering* **2021**, *7*, 424–426. [[CrossRef](#)]
2. Su, M.; Hu, B.Y.; Luan, W.X.; Tian, C. Effects of COVID-19 on China's Civil Aviation Passenger Transport Market. *Res. Transp. Econ.* **2022**, 101217. [[CrossRef](#)]
3. Zhao, Y.F.; Wan, J.Q. Analysis of Development and Evolution Rules of Civil Aviation in China Based on Life Cycle Theory. *PLoS ONE* **2019**, *14*, e0212338. [[CrossRef](#)] [[PubMed](#)]

4. Zhang, Y.; Cao, K.; Dong, W. Research on Improvement and Optimisation of Modelling Method of China's Civil Aircraft Market Demand Forecast Model. *Aeronaut. J.* **2021**, *125*, 1157–1191. [[CrossRef](#)]
5. Su, M.; Luan, W.X.; Fu, X.W.; Yang, Z.L.; Zhang, R. The Competition Effects of Low-cost Carriers and High-speed Rail on the Chinese Aviation Market. *Transp. Policy.* **2022**, *95*, 37–46. [[CrossRef](#)]
6. Qiu, X.J.; Zheng, W.H.; Tang, Y.T.; Lu, F. The Test Verification Design Method Based on Rapid Prototyping Technology of Aero-engine. *Procedia Eng.* **2015**, *99*, 981–990. [[CrossRef](#)]
7. Li, L.; Liu, Y.; Tian, L.; Hu, H.; Kohli, A. An Experimental Study on a Hot-air-based Anti-/De-Icing System for Aero-Engine Inlet Guide Vanes. *Appl. Therm. Eng.* **2019**, *167*, 114778. [[CrossRef](#)]
8. Su, L.C.; Liu, Z.X.; Lu, Y.G. Performance Research on the High-Altitude Valve of an Aero-engine Ventilation System. In Proceedings of the 2nd International Conference on Applied Mechanics and Mechanical Engineering (ICAMME 2011 Part1), Sanya, China, 8 October 2021. [[CrossRef](#)]
9. Pinto, V.T.; Cunha, M.L.; Martins, K.L.; Rocha, L.A.O.; de Vasconcellos Real, M.; dos Santos, E.D.; Isoldi, L.A. Geometric Evaluation of Steel Plates Subjected to Uniform Transverse Load with Rectangular or Trapezoidal Stiffeners by Means Constructural Design Method. *Int. J. Hydromechatron.* **2020**, *3*, 190–198. [[CrossRef](#)]
10. Balakrishna, A.; Mishra, P.K. Modelling and analysis of static and modal responses of leaf spring used in automobiles. *Int. J. Hydromechatron.* **2021**, *4*, 350–367. [[CrossRef](#)]
11. Bayat, F.; Fadaie Tehrani, A.; Danesh, M. Finite Element Analysis of Proportional Solenoid Characteristics in Hydraulic Valves. *Int. J. Automot. Technol.* **2012**, *13*, 809–816. [[CrossRef](#)]
12. Yun, S.N.; Ham, Y.B.; Park, J.H. Attraction Force Improvement Strategy of a Proportional Solenoid Actuator for Hydraulic Pressure Control Valve. In Proceedings of the 2012 12th International Conference on Control, Automation and Systems, Jeju Island, Korea, 17–21 October 2012; pp. 1123–1127.
13. Plavec, E.; Vidović, M. Genetic Algorithm Based Plunger Shape Optimization of DC Solenoid Electromagnetic Actuator. In Proceedings of the 2016 24th Telecommunications Forum (TELFOR), Belgrade, Serbia, 22 November 2016; pp. 1–4. [[CrossRef](#)]
14. Wang, L.; Li, G.X.; Xu, C.L.; Xi, X.; Wu, X.J.; Sun, S.P. Effect of Characteristic Parameters on the Magnetic Properties of Solenoid Valve for High-pressure Common Rail Diesel Engine. *Energy Convers. Manag.* **2016**, *127*, 656–666. [[CrossRef](#)]
15. Zhao, J.; Leonid, G.; Wang, Z.; Shi, Y. Influence Factors Study on the Electromagnetic Force of High Speed Solenoid Valves Used in Common Rail Injectors. *J. Harbin Eng. Univ.* **2018**, *39*, 703–708. [[CrossRef](#)]
16. Sun, Z.Y.; Li, G.X.; Wang, L.; Wang, W.H.; Gao, Q.X.; Wang, J. Effects of Structure Parameters on the Static Electromagnetic Characteristics of Solenoid Valve for An Electronic Unit Pump. *Energy Convers. Manag.* **2016**, *113*, 119–130. [[CrossRef](#)]
17. Hung, N.B.; Lim, O. Improvement of Electromagnetic Force and Dynamic Response of a Solenoid Injector Based on the Effects of Key Parameters. *Int. J. Automot. Technol.* **2019**, *20*, 949–960. [[CrossRef](#)]
18. Gao, H.L.; Zhang, F.J.; Wang, S.F.; Wu, H.; Wang, Z.K. Effect of Characteristic Parameters on the Magnetic Properties of Voice Coil Motor for Direct Fuel Injection in Gasoline Engine. *Energy Procedia* **2019**, *158*, 4184–4189. [[CrossRef](#)]
19. Zhao, J.H.; Fan, L.Y.; Liu, P.; Leonid, G. Investigation on Electromagnetic Models of High-Speed Solenoid Valve for Common Rail Injector. *Math. Probl. Eng.* **2017**, 9078598. [[CrossRef](#)]
20. Fan, L.; Zhou, W.; Liu, P.; Zhao, J.H. Multi Objective Optimization of Dynamic Response of High Speed Solenoid Valve. *J. Harbin Eng. Univ.* **2018**, *39*, 53–59. [[CrossRef](#)]
21. Lankin, M.V.; Lozin, O.I.; Lankina, M.Y. Magnetization Dynamic Characteristics Models for Hydraulic Drives of Proportional Electromagnets. *Procedia Eng.* **2017**, *206*, 443–448. [[CrossRef](#)]
22. Braun, T.; Reuter, J.; Rudolph, J. Position Observation for Proportional Solenoid Valves by Signal Injection. *IFAC-Pap. Online* **2016**, *49*, 74–79. [[CrossRef](#)]
23. Xie, F.W.; Zhou, R.; Wang, D.S.; Ke, J. Simulation Study on Static and Dynamic Characteristics of Electromagnet for Electro-Hydraulic Proportional Valve Used in Shock Absorber. *IEEE Access* **2020**, *8*, 41870–41881. [[CrossRef](#)]
24. Mozammel, M.; Asaduzzaman, R.; Farhan, T.; Munish, K.G.; Jubayer, H.; Anjan, G. Multi-objective Optimization of Chip-tool Interaction Parameters Using Grey-Taguchi Method in MQL-assisted Turning. *Measurement* **2018**, *129*, 156–166. [[CrossRef](#)]
25. Tong, L.L.; Su, C.T.; Wang, C.H. The Optimization of Multi-response Problems in the Taguchi method. *Management* **1997**, *14*, 367–380. [[CrossRef](#)]
26. Kim, S.I.; Lee, J.Y.; Kim, Y.K.; Hong, J.P. Optimization for Reduction of Torque Ripple in Interior Permanent Magnet Motor by Using the Taguchi Method. *IEEE Trans. Magn.* **2005**, *41*, 1796–1799. [[CrossRef](#)]
27. Jiang, S.J.; Chu, S.C.; Zou, F.M.; Shan, J.; Zheng, S.G.; Pan, J.S. A parallel Archimedes Optimization Algorithm Based on Taguchi Method for Application in the Control of Variable Pitch Wind Turbine. *Math. Comput. Simul.* **2023**, *203*, 306–327. [[CrossRef](#)]
28. Sahu, K.K.; Modi, Y.K. Effect of Printing Parameters on Compressive Strength of Additively Manufactured Porous Bone Scaffolds Using Taguchi Method. *Int. J. Manuf.* **2021**, *11*, 18–33. [[CrossRef](#)]